Pergamon

Int. J. Heat Mass Transfer. Vol. 40, No. 8, pp. 1753–1772, 1997

0017–9310/97 $17.00 + 0.00

PII: S0017–9310(96)00253–0

A 3-D Eulerian–Lagrangian model of dispersed flow film boiling including a mechanistic description of the droplet spectrum evolution—I. The thermal–hydraulic model

M. ANDREANI and G. YADIGAROGLU

Nuclear Engineering Laboratory, Swiss Federal Institute of Technology, ETH, ETH-Zentrum, CLT, CH-8092 Zurich, Switzerland

(*Received for publication* 16 *July* 1996)

Abstract—A hybrid Eulerian–Lagrangian model is developed to analyze dispersed flow film boiling in a vertical straight tube under typical reflooding conditions. The effect of the liquid phase on the vapour field, which is established in a two-dimensional grid, is calculated by tracking the three-dimensional trajectories of a large number of sample droplets. The detailed description of droplet hydrodynamics includes droplet size distribution, initial inertia, different mechanisms of break-up and interaction of the droplets with the wall, and the forces due to the temperature and velocity fields of the continuous phase. © 1997 Elsevier Science Ltd. All rights reserved.

1. INTRODUCTION

The study of the convective boiling of a steam–droplet mixture is of interest for industrial equipment like steam generators and reheaters. Highly disperse droplet flow in a vapour stream can also exist in a nuclear core during a hypothetical 'loss-of-coolant-accident'. Under these conditions, the liquid is not in contact with the hot wall and the calculation of the heat transfer rates is of paramount importance for the evaluation of the maximum rod surface temperature, and thus of the safety margins. A major concern is the cooling effectiveness of such a steam–droplet mixture during the reflooding phase of the postulated accident, especially under low flooding rate conditions (Fig. 1).

Recent experience with the one-dimensional (1-D) computer codes employed in safety analysis has revealed the difficulties encountered in calculating the cladding temperatures in the zones where such a dispersed flow film boiling (DFFB) regime is the prevailing heat transfer mechanism [1, 2].

Since substantial thermal and phase-velocity non-equilibrium can be present under such conditions, the appropriate modeling of interfacial mass and energy transfers is of crucial importance. The droplets act as heat sinks for the vapour and control the vapour temperature profile which, in turn, determines the wall heat transfer rate. Very high vapour superheating rates have been reported in tube experiments for low mass fluxes [3]: strong reductions of the interfacial heat transfer rates far away from the quench front, with respect to the commonly accepted theories, have been inferred by Evans *et al.* [3] from their analysis of the Lehigh University single-tube 'slow reflooding' experiments. Thus, the calculation of the thermal non-equilibrium is the major challenge for the dispersed flow film boiling models.

A recent extensive review of the prediction methods for dispersed flow film boiling including an overview of the results obtained by the most commonly used models and correlations [4] concluded that no model can be recommended for general use. Even the mechanistic models suffer from the uncertainty in the closure laws and a substantial difficulty in accounting for the droplet hydrodynamic behaviour and its influence on the vapour field.

The most common mechanistic models include a stepwise integration of the one-dimensional conservation equations for the two phases, considering heat transfer from the wall to the vapour and the droplets, as well as from the vapour to the droplets. The droplet population is represented by a unique droplet diameter determined by some 'local' criterion. Wall-to-vapour heat transfer rates are usually calculated using one of the correlations developed for single-phase gas flow and the actual vapour temperature. The degree of success of the models of this class is highly variable.

The numerous attempts to refine this basic 1-D model appear to be insufficient [4] mainly because, as recognized by Yao and coworkers [5], the thermal boundary layer is *two-dimensional*. As discussed in detail by Andreani and Yadigaroglu [1] the fundamental difficulty in modelling these phenomena by a 1-D model is due to the fact that quantities, such as the vapour velocity and temperature, droplet concentration, droplet diameter, etc., are not uniformly distributed across the channel, and the shape of their

NOMENCLATURE

A	flow area of the tube [m^2]
c_p	vapour heat capacity [kJ kg^{-1} K^{-1}]
C_D	drag coefficient
d	droplet diameter [m]
d_{32}	Sauter mean diameter (SMD) [m]
d_{50}	volume median mean diameter [m]
D	internal tube diameter [m]
G	mass flux [kg m^{-2} s^{-1}]
h	heat transfer coefficient [W m^{-2} s^{-1}]
H	specific enthalpy [kJ kg^{-1}]
k_g	molecular conductivity [W m^{-1} K^{-1}]
k_r	droplet initial radial velocity multiplier
$K_{e,k}$	droplet size reduction rate by evaporation [m s^{-1}]
m	mass [kg]
$\dot{M}$	mass flow rate [kg s^{-1}]
$\dot{N}_k$	droplet number flow rate [s^{-1}]
NR	number of Eulerian radial meshes
N_{GR}	number of droplet groups
q''	heat flux [W m^{-2}]
q''_c	convective heat flux [W m^{-2}]
q''_{dc}	direct-contact wall-to-droplet heat flux [W m^{-2}]
q''_{gf}	radiative heat flux vapour-to-liquid [W m^{-2}]
q''_{in}	net input heat flux to the wall [W m^{-2}]
q''_{rad}	radiative heat flux from the wall = $q''_{wf}+q''_{wg}$ [W m^{-2}]
q''_{wf}	radiative heat flux wall-to-liquid [W m^{-2}]
q''_{wg}	radiative heat flux wall-to-vapour [W m^{-2}]
$q'''_{rad,g}$	volumetric heat generation due to radiation [W m^{-3}]
q'''_{gi}	interfacial heat transfer rate per unit volume [W m^{-3}]
r	radial coordinate, distance from the tube axis [m]
r_I	radial location of the Ith Eulerian radial node [m]
r_k	radial position of the kth group droplet centre [m]
R_k	radius of the kth group droplet [m]
SMD	Sauter mean diameter [m]
t	time [s]
t^*	non-dimensional time
t_{BU}	non-dimensional break-up time
T	temperature [°C or K]
u	local vapour velocity (time averaged) [m s^{-1}]
U	cross-sectional average vapour velocity [m s^{-1}]
U_{fg}	cross-sectional average relative velocity [m s^{-1}]
V_I	volume of the Ith Eulerian radial mesh [m^3]
$\dot{V}$	droplet volumetric flow rate [m^3 s^{-1}]
x	quality
w	local droplet velocity [m s^{-1}]
W_z	cross-sectional average axial droplet velocity [m s^{-1}]
We	Weber number = $\rho_g U_{fg}^2 d/\sigma$
We_i	impact Weber number = $\rho_f w_r^2 d/\sigma$
z	axial coordinate [m]
$\langle\ \rangle$	average over the cross-sectional area.

Greek symbols

α_g	void fraction
α_f	liquid fraction
Γ	volumetric vapour generation rate [kg m^{-3} s^{-1}]
ΔA_w	area of the wall in the Eulerian axial mesh [m^2]
Δt	residence time [s]
ΔV_k	droplet volume loss by evaporation [m^3]
Δz	length of the Eulerian axial mesh [m]
ε_k	effectiveness of the contact
μ	dynamic viscosity [kg m^{-1} s^{-1}]
ρ	density [kg m^{-3}]
σ	surface tension [kg s^{-2}]
ϕ	angular position in the cross-sectional plane.

Subscripts

a	aerodynamic break-up
c	contact, capillary break-up
cr	critical
d	droplet
eff	effective
end	time or location at which the break-up process terminates
eq	equilibrium (for droplet population)
f	liquid
g	vapour
fg	difference between the two phases
i	interface
i,imp	impact, impact break-up
I	Ith Eulerian radial node
k	kth group of droplets
m,max	maximum
res	restitution, i.e. after contact with the wall
r	in radial direction
ref	reference
s	saturation state
t	tangential
w	wall or wave
z	in axial direction
0	at the quench front location.

Superscripts

c	in the cross-sectional plane
dc	direct contact
int	interfacial
rad	radiation
z	in axial direction
+	above quench front
−	below quench front.

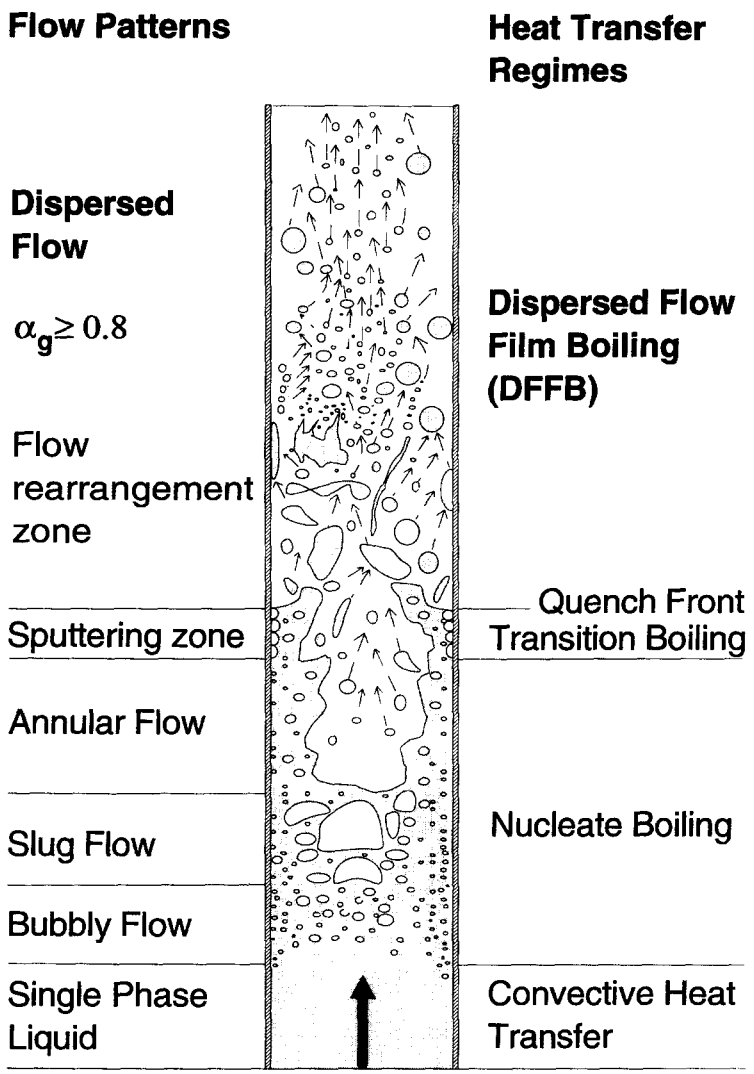

Fig. 1. Flow patterns and heat transfer regimes in a heated channel under low flooding rate conditions.

profiles is highly dependent on the initial conditions and flow history. Under such circumstances, the use of interfacial closure laws that employ cross sectional-average quantities is a fundamental limitation. A completely realistic modelling of dispersed flow film boiling is possible only if the multi-dimensional effects are considered.

A review of previous multi-dimensional models of dispersed flow film boiling is presented first. A more extensive discussion can be found in the review paper by Andreani and Yadigaroglu [4]. From the survey of the available models, it was recognized that many aspects of dispersed flow film boiling outlined above had been neglected; other aspects had been taken into account in only a crude way or using assumptions that make the model non-suitable for the description of the phenomena under reflooding conditions.

The purpose of this present work was to undertake a comprehensive attack on the mechanistic modelling and a full synthesis of the available relevant information. The importance of the processes that have not been adequately modelled is investigated by incorporating realistic submodels in a mathematical frame, especially conceived for the analysis of the specific reflooding situation. To limit the complexity of the mathematical treatment and to simplify comparisons with experimental data, the model is limited here to a simple tubular geometry; moreover, dispersed flow (void fraction $\alpha_g > 0.8$) is assumed to exist immediately above the quench front, as expected for positive quality conditions at the quench front (QF) (Fig. 1).

This approach necessarily leads to a rather complex model, which cannot be easily incorporated in a computer program of more general use. The goal of the investigation is, however, to identify the phenomena which must be accounted for a realistic simulation of dispersed flow film boiling and to provide a tentative explanation for the failure of the 1-D approach under certain conditions. Hopefully, the results of the present investigation will help define new guidelines for the improvement of the practical (necessarily 1-D) prediction methods for dispersed flow film boiling.

The comparison of the results obtained by the novel model with experimental data and extensive parametric studies are presented in a companion paper (Part II), where the 1-D results are also included and the deficiencies of the 1-D approach are discussed.

1.1. *Previous two-dimensional analyses*

The most questionable aspect [1] of most of the previous 2-D studies is the hypothesis of uniform radial droplet concentration [6, 7], which is based on experimental findings in a range that covers neither the typical conditions of dispersed flow during reflooding, nor the voidage conditions encountered in most practical applications. Moreover, experiments performed in adiabatic tubes have shown the existence of concentration profiles.

Another argument against the uniform concentration assumption comes from the studies on the trajectories of droplets entering a thermal boundary layer [8, 9]: in the region above the quench front, because of the low gas Reynolds number, only very tiny droplets could be accelerated enough in the turbulent core to penetrate the viscous layer. One would expect, however, large drops having significant radial momentum to be able to penetrate.

The first model that combines the 2-D analysis of the vapour field with the analysis of the radial migration of the droplets was proposed by Kirillov *et al.* [10]. The radial droplet concentration distribution is not imposed *a priori*; the profile evolves under the influence of the forces that act on the drop (drag, lift, added mass and buoyancy) and turbulent diffusion. The thrust force (due to non-uniform evaporation) is not included in the analysis because of the low wall temperatures typical of the applications considered (steam generators). Direct contact heat transfer is taken into consideration, while radiation is neglected.

The model of Kirillov *et al.* features a quite complete description of the droplet hydrodynamics and heat transfer processes occurring in the post-dryout zone of a steam-generator tube, under conditions of high pressure, high mass flux, moderate to high quality and low wall temperatures. It is less adequate for the study of typical reflooding situations because of the embodied assumptions: absence of radiation, neglect of the droplet break-up processes and of the thrust force. Moreover, observing the results [11] calculated for typical conditions, one realizes that the droplet concentration profile evolution is controlled by the diffusive mechanisms. This is justified for the small droplets (less than a few hundred μm), that one expects at high pressures, entrained in a strongly turbulent flow, but is not correct when large droplets are flowing in a weakly turbulent vapour velocity field. It has been shown, both experimentally [12, 13] and theoretically [13], that the effect of particle–turbulence interaction on the deposition rates of relatively *large* particles is practically negligible. Under typical reflooding conditions, large chunks of liquid are present just above the quench front and an 'equilibrium' size distribution is attained downstream of the region dominated by break-up and coalescence. In this region the average droplet diameter is not smaller than 0.5 mm. Therefore the motion of the droplets is dominated by their initial inertia at the entrainment point and by the drag and lift forces originating from their interaction with the mean velocity field and with the wall (thrust force).

Some interesting features of post-dryout heat and mass transfer are revealed by the computational experiments carried-out by Kirillov *et al.* [11]. The radial droplet concentration profile exhibits a distinct maximum in the central part of the channel, and smoothly decreases to zero at the wall. This result is supported by experimental data from annular-dispersed flow (Kirillov *et al.* [11]).

2. THE MODEL

Two main limitations affect the models presented to date: the assumption of uniform droplet concentration over the cross section or the use of a profile basically resulting from turbulent diffusion, and lack of an adequate modelling of the break-up processes. For a realistic simulation, the liquid concentration profile has to be calculated by taking into account the initial inertia of the droplets and their interactions with the vapour velocity field and with the wall. The initial size distribution of the droplet population and its evolution under the effects of break-up and evaporation have also to be considered: the effect of the presence of droplets of largely different sizes deserves special attention, since these have different histories.

The effect of the non-uniform liquid distribution on the vapour temperature field (*distributed* heat sink effect) has to be calculated taking into account the spectrum of the droplets, their velocities and their positions. Moreover, attention must be paid to the mechanism that controls the droplet generation at the quench front, as the initial axial and radial velocities, as well as the initial droplet diameter, can be critical parameters for the correct simulation of dispersed flow film boiling. Therefore the purpose of the present work is to develop a model that couples a detailed analysis of the droplet hydrodynamics with consideration of a 2-D vapour field.

This new model employs a Lagrangian description of the liquid phase and a Eulerian treatment of the vapour field: this technique, often used in combustion science and in the study of spray coolers and absorbers, has never been adopted for the fundamental study of problems related to reactor safety.

It is evident that the value of several parameters must be entered into such a model to arrive at the desired level of detail. Many of these values are largely unknown, and will be determined by analogy with similar physical situations; their importance is assessed by extensive parametric studies in the companion paper (Part II).

The initial conditions for the droplets are carefully

selected on the basis of a phenomenological description of the entrainment process: initial axial and radial velocities, as well as initial diameter of the droplets can be critical parameters of the simulation.

The computational scheme associated with the present version of the model requires specification of the total heat flux and calculates the wall temperature distribution.

3. MAJOR ASSUMPTIONS

Several assumptions are made to arrive at a tractable problem:

(a) The situation some distance downstream from the quench front changes relatively slowly, so that it is possible to use the *steady-state conservation equations.*

(b) A further important simplification is obtained by considering *constant pressure* for the high void fraction mixture flowing at low velocity (typically well below 30 m s^{-1}).

(c) Another major assumption is that *only one-way coupling exists between the velocity fields* of the two-phases: the influence of the vapour velocity on the droplet velocities is considered, but the action of the dispersed phase on the turbulent vapour-phase characteristics is neglected; a standard *fully turbulent vapour velocity profile* is used.

This last simplification is seldom justified [1], but has been adopted for simplicity, as the investigation is focussed on other, usually neglected, aspects of the process (break-up inertial deposition, radial droplet concentration profile).

Two experimental findings (reviewed in ref. [4]) are used to further simplify the equations: (1) during reflooding all the droplets generated at the quench front are carried over with a velocity that is practically independent of their size; (2) in most of the dispersed flows in channels, no radial dependence of the axial velocity has been observed over a major part of the cross section.

The consideration of two phenomena can help understand the reason of the unique 'group' velocity of the droplet swarm. Firstly, momentum exchanges due to collisions may contribute to rendering the velocities uniform; this mechanism is likely to be important at low void fractions, when the droplets have a short mean free path between collisions. A second phenomenon, well known, but never taken into consideration, is the reduction of the drag force on a particle in the wake of another particle. Experiments performed with two spheres aligned along the flow direction [14], showed that the drag coefficient for the front sphere is somewhat above the standard value for a single sphere, whereas drag on the following sphere decreases several times. Thus, the following picture can be imagined for the droplets above the quench front: small droplets are highly accelerated until they fall into the wake of a large one; at this point, the drag on the large droplet increases and that on the small droplet decreases dramatically. Their velocities tend to equalize, until a random misalignment of the two droplets renders the interaction ineffective, and the two droplets are separated again until the next interaction. As the interaction effects are felt for distances between the centres up to several times the particle diameter—six times according to the calculations of Kleinstreuer and Wang [15] for vaporizing droplets—it is clear that this effect can explain the equalization of the droplet velocities up to very high void fractions. These circumstances justify the:

(d) One-dimensional calculation of an average unique axial velocity for all the droplets.

The droplet spectrum is represented by discrete diameter groups. The calculation of the radial distribution of the liquid phase is performed by tracking the trajectories of sample droplets in a cross-sectional plane moving with the axial velocity of the droplets (Langrangian approach).

(e) The mechanism of collisions between droplets is not explicitly modelled, but *ad hoc* empirical procedures (see Section 6.3) to avoid 'negative void fractions' are used, which mimic collisional diffusion from the center of the channel towards the periphery.

Interaction between the droplets is not, however, completely overlooked, since the closure laws for drag and interfacial heat transfer take into account the packing of the droplets. Other minor, conventional assumptions are:

(f) The droplets are at saturation temperature, T_s.

(g) At the quench front, the vapour velocity profile is fully developed and the vapour is at saturation temperature.

(h) Radiation heat fluxes can be calculated using an effective droplet diameter [16]. The importance of the radiative exchanges has been shown by Peake [17] and Andreani [16].

4. VAPOUR GOVERNING EQUATIONS

Because of the constant pressure and standard *fully developed turbulent velocity profile* assumptions, the momentum equation can be put aside and the continuity and energy conservation equations suffice for establishing the velocity and temperature fields. The cross-sectional average form of the continuity equation is used to calculate the average vapour velocity U_z in a tube of diameter D and flow area A:

$$A\frac{\mathrm{d}}{\mathrm{d}z}(\langle\rho_g\rangle\langle\alpha_g\rangle U_z) = \int_A \Gamma \,\mathrm{d}A \qquad (1)$$

The vapour *axial* velocity distribution $u_z(r)$ is obtained using the imposed fully turbulent velocity profile (classical two-layer velocity distribution [18]).

The differential form of the 2-D continuity equation is then used to calculate the *radial* vapour velocity u_r:

$$\frac{1}{r}\frac{\partial}{\partial r}(r\alpha_g\rho_g u_r)+\frac{\partial}{\partial z}(\alpha_g\rho_g u_z)=\Gamma \qquad (2)$$

where Γ is the volumetric vapour generation rate (kg $m^{-3}\,s^{-1}$).

The vapour energy equation [19] is:

$$\frac{1}{r}\frac{\partial}{\partial r}(r\alpha_g\rho_g H_g u_r)+\frac{\partial}{\partial z}(\alpha_g\rho_g H_g u_z)$$
$$=\frac{1}{r}\frac{\partial}{\partial r}\left(r\alpha_g k_t\frac{\partial T}{\partial r}\right)+q'''_{rad,g}+\Gamma H_{g,s}-q'''_{gi} \qquad (3)$$

where q'''_{gi} is the interfacial heat transfer rate per unit volume (often denoted as $-Q_{gi}=Q_{ig}$) (W m^{-3}), k_t the total vapour conductivity (molecular, k_g+turbulent, k_{tur}) and $q'''_{rad,g}$ the volumetric heat source due to radiation (W m^{-3}).

Radial velocities are small, but must be considered to conserve energy when equations (1)–(3) are integrated numerically [16].

The turbulent conductivity k_{tur} is calculated, as usual [18]:

$$k_{tur}=\rho_g c_p\frac{\varepsilon_m}{Pr_{tur}}$$

where ρ_g and c_p are the vapour density and heat capacity, respectively. The eddy diffusivity ε_m is set to zero in the laminar sublayer, whereas in the turbulent core a standard relation is used [18]. The turbulent Prandtl number Pr_{tur} is calculated from:

$$Pr_{tur}=\max\left\{0.9,\frac{7000}{(Re-Re_{tr})}\right\} \qquad (4)$$

where Re_{tr} is the value of the Reynolds number at the laminar-turbulent transition (arbitrarily chosen to be equal to 2100). The empirical equation (4) produces the correct value of Pr_{tur} in the fully turbulent regime ($Pr_{tur}=0.9$ when $Re>10\,000$) and, approximately, the value suggested by Lawn [20] in the proximity of the laminar-turbulent transition ($Pr_{tur}\approx 1.5$ when $Re=7000$). For decreasing Re, an increasing Pr_{tur} yields values of the wall-to-vapour heat transfer coefficients increasingly lower than those calculated from the Dittus–Boelter correlation, as suggested by experiments [20].

The reference temperature chosen for the calculation of the transport properties and the empirical technique used to implement in the calculation the entrance length effect are discussed by Andreani [16].

The initial and boundary conditions for equations (1)–(3) are:

$$T(r,0)=T_s$$

$$\alpha_g k_m\left.\frac{\partial T}{\partial r}\right|_{r=D/2}=q''_c=q''_{in}-q''_{rad}-q''_{dc};\quad\left.\frac{\partial T}{\partial r}\right|_{r=0}=0.$$

$$U_z(0)=U_{z,0};\quad u_r\left(\frac{D}{2},z\right)=u_r(0,z)=0.$$

$$\alpha_g(r,0)=1-\alpha_f(r,0)$$

where $\alpha_f(r,0)$ is determined by the droplet hydrodynamics discussed below.

The convective heat flux q''_c is calculated by subtracting the radiative heat flux q''_{rad} and the direct wall-to-droplet heat transfer q''_{dc} from the imposed heat flux q''_{in}. The radiative heat flux from the wall q''_{rad} is the sum of the radiative heat fluxes from the wall to the droplets, q''_{wf}, and to the vapour, q''_{wg}. Radiation to the vapour is neglected as long as the optical thickness of the vapour is less than 20% of that of the liquid: for such conditions q''_{wf} is calculated by the two-flux method [17]. Otherwise, the network method [21] is used to calculate both q''_{wg} and q''_{wf} as well as the vapour-to-liquid radiative heat flux q''_{gf} (always very small).

The influence of the liquid phase on the vapour temperature is through the five terms Γ, q'''_{gi}, α_g, q''_{dc} and q''_{wf}. The droplet concentration appears in all these terms and has to be determined by solving the 3-D droplet hydrodynamics equations.

The Eulerian mesh used for calculating the vapour temperature field and the interactions between the two phases are shown in Fig. 2. Large droplets influence the field over several meshes: the way this is accounted for is described in Sections 6.3–6.4.

5. DROPLET HYDRODYNAMICS

For several two-phase flow regimes, a Eulerian approach is the most appropriate for treatment of the liquid phase. Unfortunately, many difficulties arise when droplet hydrodynamics in a conduit are studied. The droplets impact upon the wall and rebounce, so that two currents of droplets exist, one travelling towards the wall and a second travelling towards the centre. The treatment of particles travelling in opposite directions is basically incompatible with the continuum (Eulerian) approach, where a single 'average' radial velocity must be defined. The *Langrangian approach* seems to be in this case a *necessity*, and is adopted here. A fully Lagrangian calculation is fortunately not necessary, as the axial velocity has been assumed to be independent of the droplet size, and of the radial coordinate (see Section 3). The average axial droplet velocity W_z is, thus, calculated in a fixed grid and depends only on z.

Using the Lagrangian approach, the position and velocity of each group of droplets in the plane perpendicular to the tube axis (called from now on the r–ϕ plane) have to be determined. Each 'computational' droplet represents a certain number of droplets generated per unit time $\dot{N}_k$ in a multi-dimensional phase space. The total number of groups N_{GR} depends on how many initial conditions are statistically sampled.

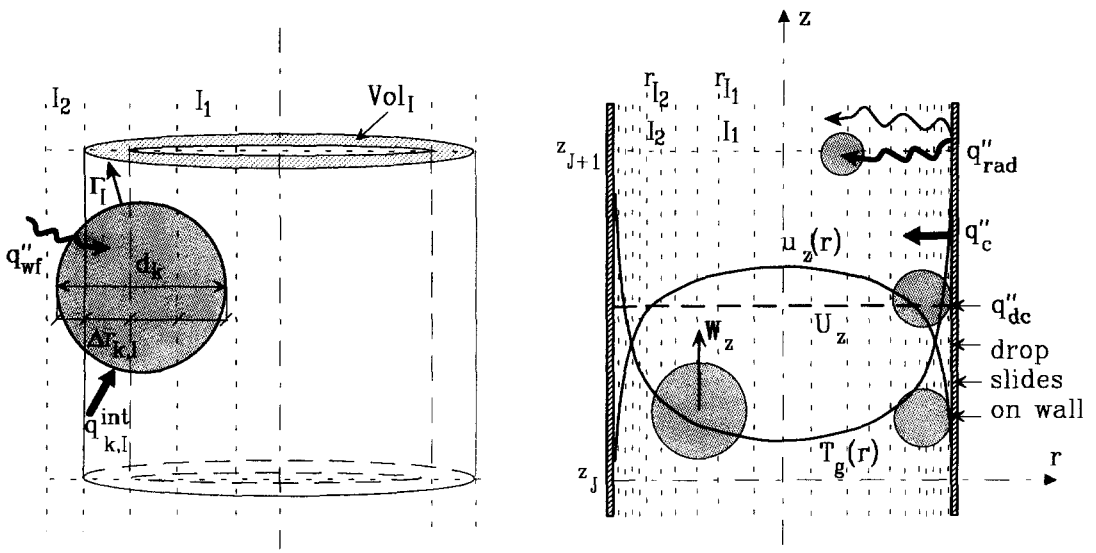

$$q^{int}_{k,I} = h_{i,k} A_k (\Delta r_{k,I}/d_k)(T_I - T_s)$$

$$Q_{ig,I} = -q'''_{gi,I} = -\sum_k q^{int}_{k,I} \dot{N}_k \Delta t_{k,I}/Vol_I$$

$$\Gamma_I = (-Q_{ig,I} + \text{radiation})/H_{fg}$$

$$I_1 \le I \le I_2$$

Interactions between the phases during residence time $\Delta t_{k,I}$. Each computational droplet represents $\dot{N}_k$ droplets/s. The droplet exchanges heat and mass with the radial cells covered by its diameter d_k.

Fig. 2. Eulerian mesh for calculating the vapour temperature field and the interactions between the phases (the thickness of the arrows indicates the importance of the various heat fluxes).

Since it is assumed that all droplets are generated at the same elevation $z = 0$ with the same initial axial velocity W_z, the initial parameters that have a statistical distribution are the radial droplet position r_k and the droplet radius R_k. In reality, the radial velocity $w_{k,r}$ the angular position ϕ_k and the tangential velocity $w_{k,t}$ of the droplets have also distributions. These are treated in a simplified manner, as discussed in Section 5.4, to limit the number of computational droplets and save computer time.

Neglecting the velocity difference between the phases in the r–ϕ plane as compared to the axial difference, the unique axial droplet velocity W_z can be calculated from a cross-sectional average momentum balance in the fixed Eulerian grid. From the formulation of Ishii and Mishima [19], neglecting pressure gradients, internal stresses and friction between the liquid and the wall,† and assuming that the distribution parameter for the momentum flux (C_{vk} in the paper above) is equal to unity, one obtains:

$$\frac{d}{dz}(\langle\alpha_f\rangle\rho_f W_z^2) = -\langle\alpha_f\rangle\rho_f g - \langle\Gamma\rangle W_z + \langle M_{if}\rangle_z \tag{5}$$

with:

$$\langle M_{if}\rangle_z = \text{interfacial drag} = -\frac{3}{4}\frac{C_D}{d_{32}}\langle\alpha_f\rangle\rho_g U_{fg}|U_{fg}| \tag{6}$$

C_D = drag coefficient (see Section 6.1)

$$d_{32} = \frac{\sum_{k=1}^{N_{GR}} \dot{N}_k d_k^3}{\sum_{k=1}^{N_{GR}} \dot{N}_k d_k^2} \tag{7}$$

U_{fg} = average relative velocity $= \langle u_z(r,z) - W_z\rangle = U_z - W_z$

$\langle\alpha_f\rangle$ = average liquid fraction

The characteristic droplet diameter used in equation (6) is the Sauter mean diameter‡ (*SMD* or d_{32}), that requires knowledge of the droplet size spectrum [23]. Equation (7) uses a 'flowing' droplet distribution (given from the number of droplets $\dot{N}_k$ of group k which cross a plane per unit time), whereas the usual definition [23] is in terms of droplet concentrations ('static' distribution). However, since it has been

† The experimental results of Watchers and Westerling [22] showed that upon impact with the wall only the radial component of the droplet velocity is reduced.

‡ The Sauter mean diameter is the correct length scale as the axial rate of momentum change of the liquid per unit volume in proportional to the sum of the drag forces acting on the droplets ($\propto \Sigma_{k=1}^{N_{GR}} d_k^2$) and inversely proportional to the total liquid volume ($\propto \Sigma_{k=1}^{N_{GR}} d_k^3$).

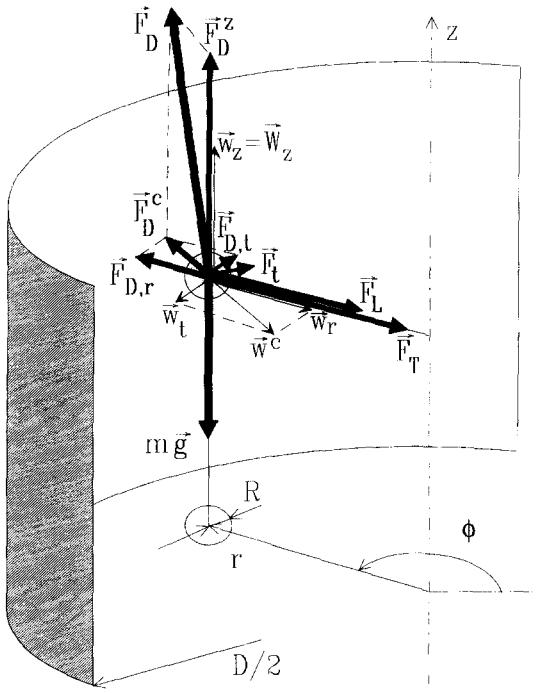

Fig. 3. Droplet velocity components and forces acting on the droplets.

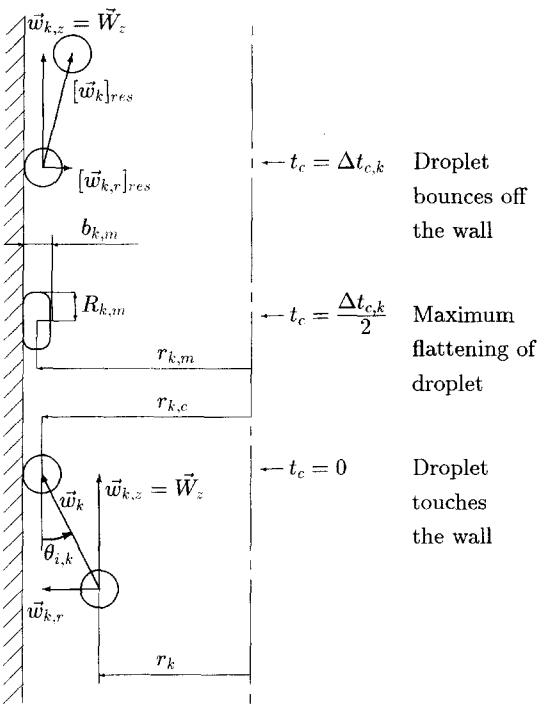

Stable droplet: $We_{i,k} < We_{i,cr}$

Fig. 4. Wall–droplet impact dynamics.

assumed that $w_{k,z}$ is the same for all droplet groups, concentrations and number flows are scaled by a constant, independent of k: therefore, either the 'static' or the 'flowing' distribution can be used to calculate the Sauter mean diameter.

Since break-up and collisions do not take place during a calculational time step, and the evaporation rate is low enough, the variation of the droplet mass in the momentum equation in the r–ϕ plane is neglected. The position $\mathbf{x}_k \equiv (r_k, \phi_k)$ and velocity $\mathbf{w}_k^c \equiv (w_{k,r}, w_{k,t})$ of each droplet group† in the r–ϕ plane (see Fig. 3) are calculated from:

$$\frac{d}{dt}\mathbf{x}_k = \mathbf{w}_k^c \tag{8}$$

$$m_k \frac{\mathrm{d}}{\mathrm{d}t}\mathbf{w}_k^c = \mathbf{F}_{D,k}^c + \mathbf{F}_{L,k} + \mathbf{F}_{t,k} + \mathbf{F}_{T,k} \tag{9}$$

where:

- $\mathbf{F}_{D,k}^c$ = component of the drag force in the r–ϕ plane;
- $\mathbf{F}_{T,k}$ = thrust force;
- $\mathbf{F}_{L,k}$ = lift force;
- $\mathbf{F}_{t,k}$ = 'turbulent' force in the r–ϕ plane.

Equations (8)–(9) are valid as long as the distance of the centre of a droplet from the wall is larger than its radius. When contact occurs ($r_k = r_{k,c} = D/2 - R_k$), a simplified description of the collision dynamics is employed: Fig. 4 illustrates how the impact dynamics is treated in the present model. It is generally accepted that the contact time $\Delta t_{c,k}$ is approximately equal to the first-order vibration period of a freely oscillating droplet (e.g. ref. [24]):

$$\Delta t_{c,k} \approx \pi \sqrt{\frac{\rho_f R_k^3}{2\sigma}} \tag{10}$$

It is also known [24] that the behaviour of a droplet impinging on a hot wall is mainly controlled by the so-called impact Weber number:

$$We_{i,k} = \frac{\rho_f w_{k,r}^2 d_k}{\sigma} \tag{11}$$

The contact time (equation 10) is made dependent on the $We_{i,k}$ (according to Kendall's results [25]), and is further reduced by a factor of 2 for unstable droplets (i.e. when $We_{i,k} > We_{i,cr}$, as discussed below), to take into account the shorter contact time of a breaking droplet [22].

If $We_{i,k} < We_{i,cr}$, the droplet assumes the shape of a flat globule (Fig. 4) and slides on the wall at the average droplet velocity W_z. The radius of the contact area increases, reaches a maximum $R_{k,m}$ (calculated from an equation developed by Kendal [25]), and decreases, until the time the droplet takes a quasi-spherical shape again and bounces off the wall.

The droplet radial velocity is first decreased linearly to zero, and after the position of the droplet centre reaches its maximum $r_{k,m}$, it is inverted. At the end of

† Position and velocity are referred to the centre of the droplet, assumed spherical.

the contact time, the radial velocity $[w_{k,r}]_{res}$ can be calculated using the experimental results presented graphically by Bolle and Moureau [26]. In their experiments, the impact was normal to the surface, and $We_{i,cr} \approx 70$. In the present model, the value of $We_{i,cr}$ is assumed to depend on the impact angle (see Section 5.3.2, below).

During the contact time, the tangential velocity $w_{k,t}$ is not updated, and at the end of the contact it is randomly assigned a value within 10% from that at the beginning of the contact (slightly off-normal bouncing).

5.1. *Forces acting on the droplets*

Analytical expressions for the forces acting on the droplets in the r–ϕ plane are given in this section. An analysis of the order of magnitude of these forces and of the stopping distances for a 1 mm droplet under the typical conditions investigated in the present study is given by Andreani [16]. It was concluded that thrust and lift forces are equally effective in preventing droplets from depositing on the wall. They can stop, however, the movement of the droplet in the r–ϕ plane, only after it has crossed the tube a few times and lost most of its initial r, ϕ momentum under the effect of the drag force.

Drag force. The first term on the right hand side of equation (9) is the projection of the drag force acting on the droplets of group k on the r–ϕ plane. For each droplet group the drag force is calculated as:

$$\mathbf{F}_{D,k} = \tfrac{1}{2}\rho_g C_D A_{d,k} |\mathbf{u} - \mathbf{w}_k| (\mathbf{u} - \mathbf{w}_k)$$

and its component in the cross-sectional plane is:

$$\mathbf{F}^c_{D,k} = \tfrac{1}{2}\rho_g C_D A_{d,k} |\mathbf{u} - \mathbf{w}_k| (\mathbf{u}^c - \mathbf{w}^c_k) \qquad (12)$$

where the drag coefficient is calculated according to the prevailing droplet flow regime (see Section 6.1).

Turbulent force. The effect of turbulence on the particles is taken into account by considering the random fluctuations of the vapour velocity field and of the resulting additional drag: such a 'turbulent' force is calculated according to a technique devised by Dukowicz [27]. For the relatively large droplets which are mostly encountered in the post-critical-heat-flux region at low pressures, such a force was found to play a minor role [16].

Lift force. A particle moving in a fluid having a non-uniform velocity experiences a lateral lift force. Although Saffman [28] derived an expression for the lift force under very restrictive conditions (small particles, low particle Reynolds number, free uniform shear flow) many researchers have applied his analysis to explain the lateral migration of small particles across streamlines in Poiseuille flow and other bounded flows. This is mainly because there is no other theoretical result for the lift on a particle due to a velocity gradient. Rizk and Elgobashi [29] justify the use of Saffman's expression in the wall region, considering that in vicinity of the wall the fluid velocity distribution is linear and, thus, a particle is subjected to a uniform shear. This point of view is supported by the experimental results of Hall [30], who showed that measured lift forces on large stationary particles (particle Reynolds number up to several hundreds) suspended at different distances from a wall are matched within a factor of 2 by Saffman's theoretical expression. Therefore, the Saffman expression for the lift force was also used in the present work:

$$\mathbf{F}_{L,k} = 1.6 d_k^2 \sqrt{\rho_g \mu_g \frac{\mathrm{d}u_z}{\mathrm{d}r}} [u_z - W_z]\mathbf{n} \qquad (13)$$

where $\mathbf{n}$ is the unit vector perpendicular to the wall. The direction of the lift force is such that a sphere lagging behind the fluid migrates away from the wall, while a sphere leading the fluid migrates in the opposite direction.

In the present analysis the lift force is allowed to act on all the droplets with diameter smaller than the tube radius, independently of their position, as long as the gas Reynolds number is lower than 10^4, i.e. below the value for fully turbulent flow.

Thrust force. As observed by Ganic and Rohsenow [8], an additional force is associated with drop motion in dispersed flow film boiling: because of the temperature gradient in the thermal boundary layer, the side of the droplet closer to the wall evaporates at a higher rate and vapour is produced at higher velocity than on the 'cold' side. This produces a reaction or thrust force which tends to prevent the deposition of the droplet on the wall.

Lee and Almenas [9] consider as thermal boundary layer the thickness of the laminar-like region (the region where the motion of the particles is controlled by forces proportional to the mean shear). They show that, already for droplets of a few tens of microns, such a region extends over the whole tube area, so that, for droplets sufficiently large, a reaction force proportional to the local temperature gradient is to be expected at any distance from the wall. Moreover, the authors proposed to use for the velocity of the evaporating vapour the r.m.s. velocity of vapour molecules at saturation temperature $\langle v_K \rangle$. This produces a sufficiently large thrust force expressed by:

$$\mathbf{F}_{T,k} = \langle v_K \rangle \frac{h_{i,k}}{H_{fg}} \frac{\pi}{8} d_k^3 \frac{\mathrm{d}T}{\mathrm{d}r}\mathbf{n} \qquad (14)$$

where $h_{i,k}$ is the interfacial heat transfer coefficient and $\langle v_K \rangle$ is calculated from the classical kinetic theory of gases:

$$\langle v_K \rangle = C_n \left(\frac{3K_B T_s}{m}\right)^{1/2} \qquad (15)$$

where K_B is the Boltzmann's constant (1.38062×10^{-23} J K^{-1}) and m is the mass of a gas molecule (2.9916×10^{-26} kg for vapour). The factor C_n ($=0.64$) is introduced to consider the component of the velocity of the gas molecules perpendicular to the wall.

5.2. *Droplet radius reduction rate*

Making the usual assumption that all the heat transferred to a saturated droplet, q_k, is used to produce vapour, the volume loss due to evaporation may be written as:

$$\frac{\mathrm{d}}{\mathrm{d}t}V_k = 4\pi R_k^2 \frac{\mathrm{d}}{\mathrm{d}t}R_k = -\frac{q_k}{\rho_\mathrm{f} H_\mathrm{fg}}$$

from where:

$$\frac{\mathrm{d}}{\mathrm{d}t}R_k = -\frac{q_k}{4\pi R_k^2 \rho_\mathrm{f} H_\mathrm{fg}} = -K_{\mathrm{e},k}. \tag{16}$$

The evaporation rate, or alternatively the droplet radius reduction rate $K_{\mathrm{e},k}$ is the sum of three contributions: radiation, interfacial heat exchange with the vapour and direct heating from the wall. Thus:

$$K_{\mathrm{e},k} = K_{\mathrm{e},k}^{\mathrm{rad}} + K_{\mathrm{e},k}^{\mathrm{int}} + K_{\mathrm{e},k}^{\mathrm{dc}} \tag{17}$$

The *contribution due to radiation* is calculated by assuming that the heat E_k^{rad} absorbed by a droplet during its total residence time in the Eulerian mesh Δz is independent of its radial position. The partition of the total power radiating from the wall among the droplet groups is, thus, only dependent on the droplet size. In the present model, the radiative flux is transferred to each group in proportion to its volumetric flow rate: this choice has been discussed by Andreani [16]. Therefore, E_k^{rad} is equal to the total energy radiating from the wall times the ratio between the volume of the droplets and the total volume of liquid that has crossed the computational mesh Δz in the time Δt:

$$E_k^{\mathrm{rad}} = q''_{\mathrm{wf}} \cdot \Delta A_\mathrm{w} \cdot \frac{V_k}{\dot{V}_\mathrm{f}} \tag{18}$$

where:

$$\dot{V}_\mathrm{f} = \sum_{k=1}^{N_{\mathrm{GR}}} \dot{N}_k \cdot V_k$$

$= $ total liquid volumetric flow ($\mathrm{m}^3\ s^{-1}$)

$\Delta A_\mathrm{w} =$ area of the wall in the Eulerian axial mesh

$$= \pi D \Delta z$$

Thus:

$$q_k^{\mathrm{rad}} = \frac{E_k^{\mathrm{rad}}}{\Delta t} = q''_{\mathrm{wf}} \cdot \Delta A_\mathrm{w} \cdot \frac{V_k}{\dot{V}_\mathrm{f} \cdot \Delta t} \tag{19}$$

where

$$\Delta t = \frac{\Delta z}{W_z} \tag{20}$$

is the transit time of the droplets in the mesh Δz, and

$$K_{\mathrm{e},k}^{\mathrm{rad}} = \frac{q''_{\mathrm{wf}} \cdot \Delta A_\mathrm{w}}{\dot{V}_\mathrm{f} \cdot \rho_\mathrm{f} \cdot \Delta t \cdot H_\mathrm{fg}} \cdot \frac{R_k}{3} = \frac{\pi D q''_{\mathrm{wf}} \cdot W_z}{\dot{V}_\mathrm{f} \cdot \rho_\mathrm{f} \cdot H_\mathrm{fg}} \cdot \frac{R_k}{3} \tag{21}$$

The *contribution due to interfacial heat transfer* is easily derived:

$$q_k^{\mathrm{int}} = h_{\mathrm{i},k} \cdot A_k \cdot (T_{\mathrm{eff}} - T_\mathrm{s}) \tag{22}$$

where A_k is the surface area of the computation droplet. Therefore:

$$K_{\mathrm{e},k}^{\mathrm{int}} = \frac{h_{\mathrm{i},k} \cdot (T_{\mathrm{eff}} - T_\mathrm{s})}{\rho_\mathrm{f} \cdot H_\mathrm{fg}} \tag{23}$$

The 'effective' vapour temperature T_{eff} that appears in the equation above is a simple average over the radius in the radial meshes covered by the droplet:

$$T_{\mathrm{eff}} = \frac{1}{r_{k,\mathrm{L}} - r_{k,\mathrm{R}}} \int_{r_{k,\mathrm{R}}}^{r_{k,\mathrm{L}}} T(r)\,\mathrm{d}r \tag{24}$$

where $r_{k,\mathrm{L}}$ and $r_{k,\mathrm{R}}$ are the 'limits' of the droplet defined further in Section 6.3.

The droplet is assumed to exchange *heat directly with the wall* when the distance of its centre from the wall is smaller than its radius. The effectiveness of the contact ε_k is defined as the ratio between the heat exchanged E_k^{dc} and that necessary to evaporate completely the droplet:

$$\varepsilon_k = \frac{E_k^{\mathrm{dc}}}{\rho_\mathrm{f} \cdot H_\mathrm{fg} \cdot V_k} \tag{25}$$

If the heat transfer rate during the contact time $\Delta t_{\mathrm{c},k}$ is considered constant, the heat exchanged per unit time is:

$$q_k^{\mathrm{dc}} = \frac{\varepsilon_k}{\Delta t_{\mathrm{c},k}} \cdot \rho_\mathrm{f} \cdot H_\mathrm{fg} \cdot V_k \tag{26}$$

and

$$K_{\mathrm{e},k}^{\mathrm{dc}} = \frac{\varepsilon_k}{3 \cdot \Delta t_{\mathrm{c},k}} \cdot R_k. \tag{27}$$

The effectiveness of the impact on a dry wall (wall temperature T_w higher than the quench temperature) is evaluated from the equation derived theoretically by Kendall [25] for heat transfer to the bottom of a flat cylindrical drop, multiplied by a factor 1.5, to account for the additional heat transfer to the sides [31]. The Kendall expression yields increasing values of the effectiveness for increasing values of $We_{\mathrm{i},k}$ and T_w; ε_k is in the range between 0.001 and 0.003 for a wide range of conditions. However, Ueda [24] found much higher values (0.005–0.007) at low wall temperatures, i.e. for T_w up to $T_\mathrm{s}+120\mathrm{K}$. Thus, an interpolation procedure was developed [16] combining the high effectiveness at low wall superheating (close to the quench front) of Ueda with the low effectiveness calculated from Kendall's equation for high T_w. The 'break' point was defined by the quench temperature calculated from the correlation of Yao and Cai [32], where it depends on the impact angle $\theta_{\mathrm{i},k}$ (Fig. 4).

5.3. *Droplet break-up*

The inclusion of droplet break-up in a dispersed flow film boiling model is one of the most original contributions of this investigation. Some experimental evidence suggests that break-up phenomena can occur over significant portions of the total length of the channel. The few models that take this process into account assume that capillary break-up splits the parent droplet in two pieces, or define the Sauter mean diameter as function of the distance from the quench front [33]. The visual experiments of Ardron and Hall [33] have shown that some capillary break-up does indeed take place, and this process leads to the splitting of slender liquid globules (or filaments) in a few large fragments. More often, however, the large droplets undergo fragmentation by aerodynamic break-up, and the most common break-up mode (the bag mode) produces a swarm of small droplets, which can be characterized by an upper-limit-log-normal distribution.

Though there is no explicit evidence that droplets flowing above the quench front break upon impinging on the wall, it is quite likely that this happens for big droplets having a sufficiently large radial velocity. Several experiments [22] have shown that droplets having sufficient radial momentum splatter onto the wall and disintegrate into small fragments.

Although break-up mechanisms, other than the ones mentioned here, are also known (splitting upon interaction with a turbulent fluctuation, break-up after collision), these are not expected to be important and only three break-up modes are considered in this work:

- aerodynamic break-up;
- wall-impact break-up;
- capillary break-up.

5.3.1. *Aerodynamic break-up.* No detailed mechanistic models are available for the aerodynamic break-up process, but a few experimental investigations [34, 35] provided useful information. The volume spectrum of the droplets generated from a fragmentation process is generally well approximated [36, 37] by an upper-limit-log-normal distribution:

$$\frac{\mathrm{d}V}{\mathrm{d}y} = \frac{\delta}{\sqrt{\pi}} \mathrm{e}^{-\delta^2 y^2} \tag{28}$$

with:

$$y = \ln\left(\zeta \frac{d}{d_\mathrm{m} - d}\right)$$

ζ and δ being the distribution coefficients, which define the volume median diameter† d_{50} and the deviation about the mean, δ, respectively:

$$\zeta = \frac{d_\mathrm{m} - d_{50}}{d_{50}}; \quad \delta = \left[4 \ln\left(\frac{d_\mathrm{m} - d_{32}}{\zeta d_{32}}\right)\right]^{-1/2}$$

where d_m is the diameter of the largest fragment. The upper-limit-log-normal distribution is thus determined by three characteristic sizes (d_{50}, d_{32} and d_m). Using the experimental findings discussed by Pilch and Erdman [35] and observing that the ratio between the Sauter mean diameter d_{32} and the d_m in the tube reflooding experiments of Ardron and Hall [33] was in the range 1/3–1/2, it is assumed that:

$$d_{\mathrm{a},50} = \tfrac{1}{2} d_{\mathrm{a,m}}, \quad d_{\mathrm{a},32} = \tfrac{1}{3} d_{\mathrm{a,m}}$$

where the subscript 'a' refers to aerodynamic break-up. Under these assumptions, the value of the largest droplet diameter after break-up $d_{\mathrm{a,m}}$ fully characterizes the spectrum of the daughter droplets.

The value of $d_{\mathrm{a,m}}$ is not known with precision, but it has been reported to depend on the Weber number:

$$We = \frac{\rho_\mathrm{g} U_\mathrm{fg}^2 d}{\sigma}$$

It ranges between 0.1 and 0.2 times the diameter of the parent drop for $We \approx 10$–20 [38]. For each computational droplet k that breaks up, the value $d_{\mathrm{a,m},k} = 0.2 d_k$ was adopted in this study.

The break-up process is not instantaneous, and large deformations of the droplets are required before the fragmentation occurs ([35], Fig. 5). Break-up times depend on the Weber number [34] and, at low We, are of the order of a few tens of milliseconds. Because of this delay in fragmentation, the large droplets travel a certain distance before disintegrating, with obvious consequences on the heat and momentum transfer mechanisms. There is general agreement [38] that the non-dimensional break-up time (or distance travelled by the droplet):

$$t_{\mathrm{BU},k} = \sqrt{\frac{\rho_\mathrm{g}}{\rho_\mathrm{f}}} \frac{2}{d_k} \int_{t_{\mathrm{crit},k}}^{t_{\mathrm{break\text{-}up},k}} (U_z - W_z)\, \mathrm{d}t \tag{29}$$

lies in the range 2.5–6.5, $t_{\mathrm{crit},k}$ being the time when $We_k > We_{\mathrm{cr},k}$. On the contrary, the value of the critical Weber number for the different aerodynamic break-up modes is still a matter of discussion. Published values vary between 2.25 and 22, since the stability of the droplets is also influenced by their acceleration rate [38] and impulsive forces [39]. Parametric studies are thus necessary (Part II). The break-up process is represented in the model in the following way (Fig. 5).

(1) The droplet of diameter d_k reaches the unstable condition when its Weber number (calculated for all droplet groups using the unique axial droplet velocity W_z and the *average*‡ axial vapour velocity U_z), We_k

† The volume median diameter d_{50} is defined from the condition that 50% of the liquid volume is carried by droplets of $d < d_{50}$.

‡ The droplet being relatively large, it does not make much sense to consider the *local* vapour velocity.

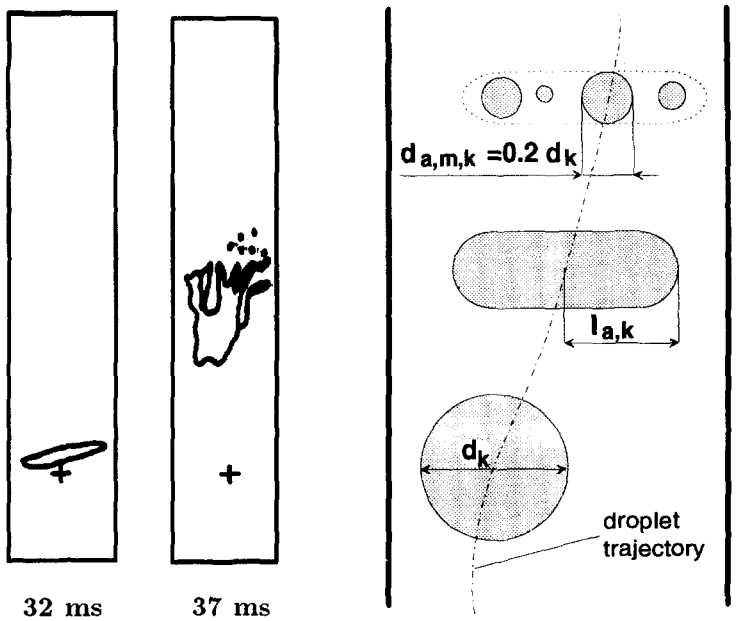

Fig. 5. Observed (left) aerodynamic break-up in a tube [33] and its representation in the model (right).

$= \rho_g(U_z - W_z)^2 d_k/\sigma$, reaches a critical value which is input to the model (base case $We_{cr} = 12$).

(2) For each droplet that has reached this critical condition, the cumulation of a non-dimensional time t_k^* (defined by equation (29), with $t_{\text{break-up},k}$ replaced by the current time) is initiated. The deformation process (Fig. 5) is described in Section 6.3.

(3) The non-dimensional break-up time $t_{BU,k}$ is randomly chosen at the beginning of the calculation from a uniform distribution within the range 2.5–6.5.

(4) When $t_k^* > t_{BU,k}$ break-up occurs.

(5) The droplets generated by break-up are divided in four groups: the upper-limit-log-normal distribution, equation (28), is used. The maximum diameter of the fragments $d_{a,m,k}$ is again equal to 0.2 d_k.

(6) The four newly generated droplets are randomly placed within the space occupied by the parent drop and their radial and tangential velocities are those of the droplet just before break-up.

5.3.2. *Wall-impact break-up.* Experiments where droplets are forced to impinge normally (or at small angles from the perpendicular) on the wall, show that for $We_{i,k} < 30$, practically no break-up occurs. If $We_{i,k}$ (equation 11) is larger than $We_{i,cr} \approx 50$–80, the droplet forms a thin liquid film that disintegrates in tiny droplets soon after the contact (Fig. 6); in this case the contact time is much shorter than that given by equation (10). In an intermediate range of $We_{i,k}$, a certain fraction of droplets break up only after moving away again from the hot surface, ejecting a few droplets only.

Yao and Cai [32] observed that, for an impact angle $\theta_{i,k}$ smaller than 60° (see Fig. 6) $We_{i,cr}$ can be reduced dramatically. Their value of the critical impact Weber number adopted here is given by:

$$We_{i,cr,k} = 12.89 + 0.85\theta_{i,k} - 0.0053\theta_{i,k}^2 \quad (30)$$

where $\theta_{i,k}$ is in degrees. The details of the break-up process are not known; therefore it is assumed that the largest fragment has a diameter $d_{i,m}$ corresponding to the minimum thickness of the film $b_{k,m}$ (Fig. 6) during the splattering process. The fragment size spectrum is assumed to be described by an upper-limit-log-normal distribution with $SMD_i = 1/3(d_{i,m})$ and $d_{i,50} = 1/2(d_{i,m})$ by analogy with the aerodynamic break-up process discussed above.

5.3.3. *Capillary break-up.* Capillary break-up, which leads to the fragmentation of the parent drop into a few large fragments (Fig. 7), has been introduced into the model to get a reduction of the average droplet size above the quench front also *under low mass flux conditions.* Under such conditions, the large droplet (several mm) expected at the quench front (see Section 5.4) are always stable against both wall and aerodynamic break-up. Thus, unless another break-up mechanism is postulated, the droplets decelerate (and the void fraction decreases) up to locations very far from the quench front. This unrealistic situation can be avoided by reducing the Sauter mean diameter of the droplet population by capillary break-up, so that the droplets can be carried-over, as physically expected. Moreover, this reduction was necessary to get agreement between calculated and experimental wall and vapour temperatures, as discussed in detail in the companion paper (Part II).

Obviously, another solution would have been to use a smaller initial Sauter mean diameter for low mass flux conditions: no correlation was found, however, which can produce either large or small initial Sauter mean diameter, depending on the initial conditions ([16]; see also Part II).

Capillary break-up is expected to be caused by the impulsive forces acting on the droplets immediately above their entrainment location, where they are sud-

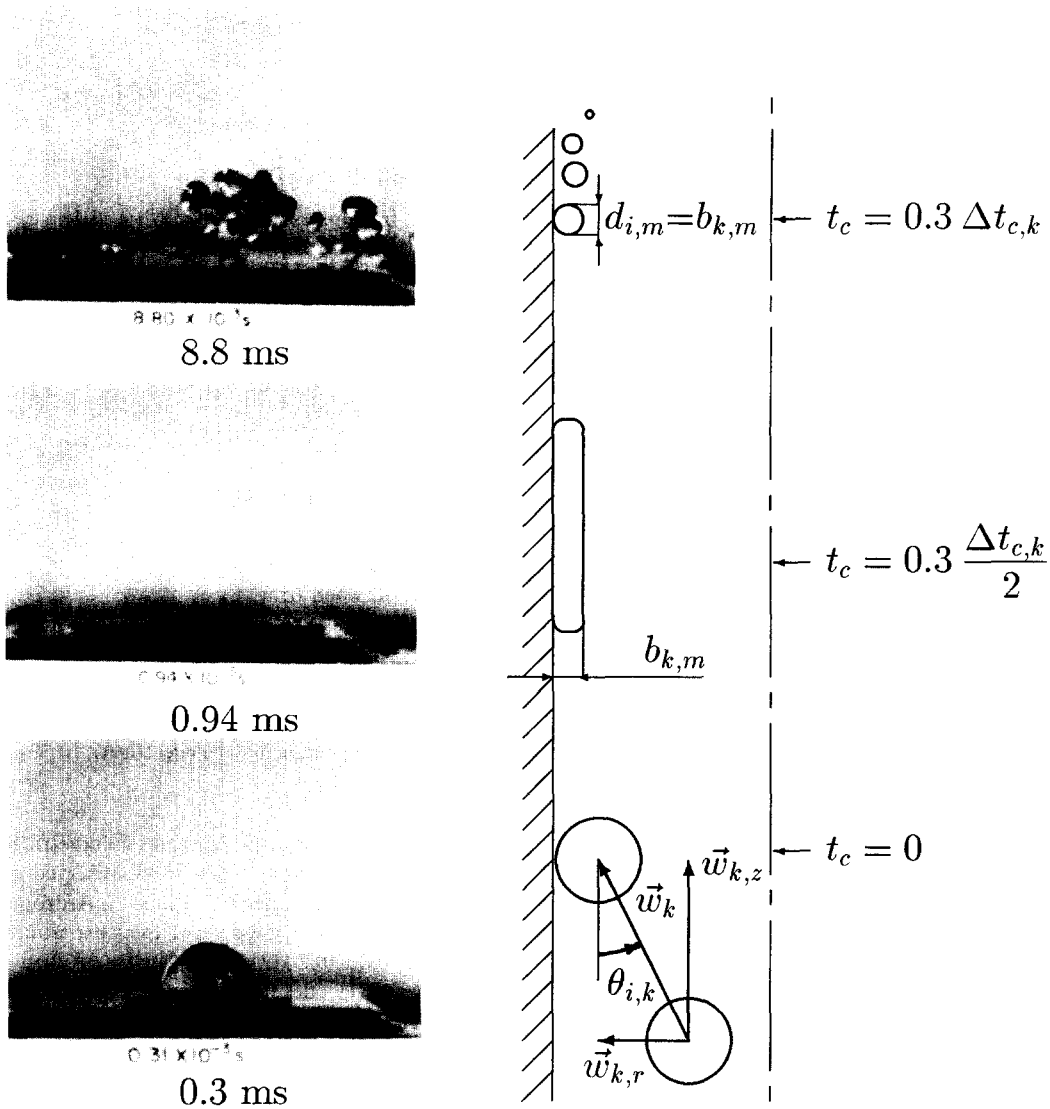

Fig. 6. Observed (left) wall impact break-up on a flat wall (reproduced with permission from Elsevier Science Ltd) and its representation in the model (right).

denly exposed to a high velocity gas field; these forces decay to zero when the condition of mechanical equilibrium is reached. It is further assumed that such a mechanical equilibrium condition is reached (and capillary splitting terminates) when the Sauter mean diameter of the droplet population reaches a mechanical equilibrium value, SMD_{eq}, obtained from a balance between drag and gravity forces. Capillary break-up is modelled according to the following *empirical* procedure (summarized in Fig. 7):

(1) The equilibrium diameter SMD_{eq} is calculated by balancing gravity and drag forces acting on a droplet, using the average gas and liquid velocities *at the quench front*. The largest droplet in the equilibrium distribution is assumed to have $d_{m,eq} = 3SMD_{eq}$.
(2) An equilibrium We_b equal to twice the initial Weber number $We_{m,0}$ of the largest droplet (of diameter $d_{m,0}$) at the quench front is calculated. The value of We_b is empirically limited in the range 1–2.5. The same range of values for the critical Weber number was suggested by Kataoka *et al.* [40] for turbulent break-up.
(3) As soon as a droplet reaches the condition $We_k > We_b$, it produces two groups of daughters. The volume distribution of the fragments is again an upper-limit-log-normal distribution, with the maximum at $d_{m,eq}$ given above the $SMD_c = 1/3(d_{m,eq})$, $d_{c,50} = 1/2(d_{m,eq})$. Additional details are given in Fig. 7.

Capillary break-up is not allowed if $We_{m,0}$ is within 30% from We_{cr}, as, under these circumstances, aerodynamic break-up is the prevailing fragmentation mechanism. However, for initial radial droplet velocities sufficiently high and producing wall-impact break-up, the procedure above has been slightly modi-

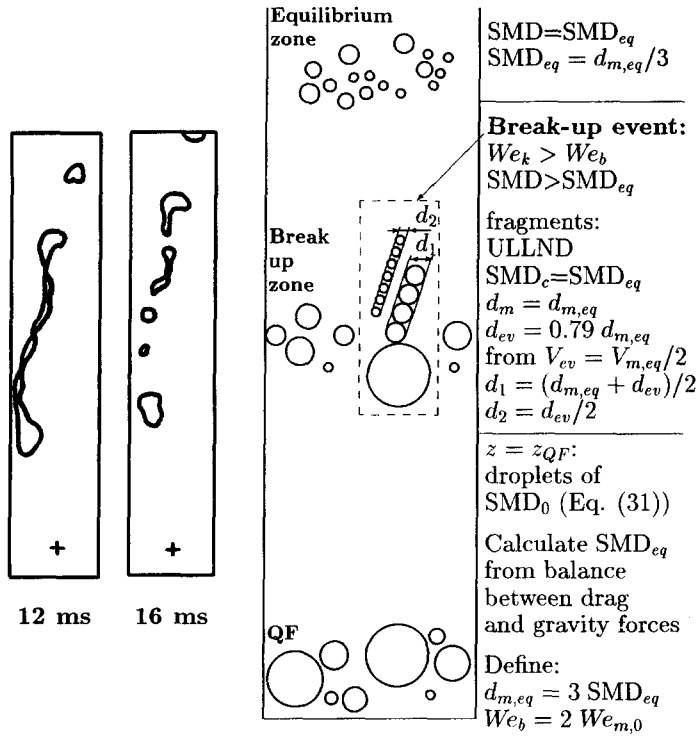

Fig. 7. Observed (left) capillary break-up in a tube [33] and its representation in the model (right).

fied to ensure a continuous dependency of the equilibrium droplet diameter on the initial radial velocity [16].

In all the experimental runs analyzed, the capillary break-up process was complete within 30–50 cm from the quench front. Capillary break-up has, however, been seldom observed [33] and its importance here is probably exaggerated. The model is *not* intended for general use, as its parameters resulted from an *ad hoc* data-fitting approach rather than from experimental observations.

5.4. *Initial conditions*

A number of flow conditions must be specified at the upstream boundary of dispersed flow film boiling. Their specification is discussed in this section.

5.4.1. *Initial size and position of the droplets.* From their visual experiments, Ardron and Hall [33] concluded that the shearing off of large waves from the liquid film below the quench front was the most important entrainment mechanism. The Sauter mean diameter of the droplet population was calculated from the volume of water carried by each individual disintegrating wave (travelling with speed c_w) as:

$$\frac{SMD_0}{\left[1-\left(\frac{SMD_0}{D}\right)^2\right]^{1/3}} = C\left[\frac{1500A}{\pi c_w}\right]^{1/3}\left[\frac{j_{f,0}\sigma}{\rho_g j_g^2}\right]^{1/3} \quad (31)$$

where A is the flow area and j denotes volumetric flux. Using $C = 0.52$ and $c_w = 2$ m s^{-1} (the observed wave velocities were in the range 1.5–3 m s^{-1}), Ardron and Hall obtained a fairly good fit of their experimental results ($x = 0.05$–0.25, $G = 19$–74 kg m^{-2} s^{-1}).

Equation (31), developed from experiments at atmospheric pressure, is used in this investigation to calculate the initial Sauter mean diameter for all conditions investigated (pressure up to 7 bar). For the conditions analyzed (see Part II), SMD_0 is in the range between 2 and 8 mm. The maximum size of the droplets is given using reasonable limits:

$$d_{m,0} = \min(0.95D, 3SMD_0) \quad (32)$$

Having determined SMD_0, an upper-limit-log-normal distribution for the droplet volume distribution, equation (28), is assumed. This happens to fit adequately the data of Ardron and Hall. The droplet size spectrum is divided in NM segments at 1 mm intervals. The (assumed) smallest droplet diameter in the spectrum ($d_0 = 10$ μm), sets a lower limit to the logarithmic distribution. The first segment (10 μm–1 mm) is further subdivided in four ranges at 100, 250, 500 and 1000 μm. The total number of segments NS is, therefore, equal to $NM+3$.

For each initial droplet radius $R_{k,0}$, a number ND of computational particles ($ND = 10$ in the reference calculations) is used; this is to distribute the radial position of the droplet centres $r_{k,0}$ in the cross section. The volumetric flow rate $\dot{V}_{k,0}$ assigned to each computational droplet† is then:

† The total number of computational droplets ($NS \times ND$) depends on the diameter of the largest droplet and is in the range 100–170.

$$\dot{V}_{k,0} = \dot{V}_f \cdot f_1(r) \cdot f_2(R) \quad k = 1, \ldots, N_{GR} \quad (33)$$

where $\dot{V}_f$ is the total volumetric liquid flow rate and f_1 and f_2 are distribution functions. The exact definition of f_1 is not important since the droplets are rapidly redistributed; f_1 is taken to be equal to $1/ND$. The function f_2 is obtained from:

$$f_2 = \int_{d_{i-1}}^{d_i} \frac{dV}{dy} dy; \quad i = 1, \ldots, NS$$

where dV/dy is given by equation (28). The number flux of droplets of group k, $\dot{N}_k$, can be calculated from the volumetric flow rate $\dot{V}_{k,0}$: fractional numbers of droplets *are* allowed. $\dot{N}_k$ does not change along the trajectory of the droplet, as long as break-up does not occur.

5.4.2. *Axial velocity*. The initial axial velocity of all the droplets is assumed to be equal to the speed of the fastest growing wave c_w [41] on the liquid film below the quench front. The average speed of the film W_z^- is found from the void fraction below the quench front, $\langle \alpha_g \rangle^-$, calculated for the quality x^- below the quench front from a steady-state heat balance, using the drift flux correlation for churn-turbulent flow for Ishii [42]. Ishii's correlation was preferred to other alternatives [43] because it was able [16] to predict the void fractions below the quench front measured by Kawaji in tube reflooding experiments [44].

The quality above the quench front, x^+, is calculated by a standard procedure taking into account the sensible heat released from the wall to the fluid during the quenching process [45].

The droplet axial velocity is assumed not to change between the elevations just below and above the quench front, so that from $W_{z,0} = W_z^- = c_w$ and x^+, $U_{z,0} \equiv U_z^+$ and $\langle \alpha_{g,0} \rangle \equiv \langle \alpha_g \rangle^+$ can also be calculated.

5.4.3. *Radial velocity*. Since there is no information about the initial radial velocities of droplets generated during a reflooding process, it is reasonable to assume that a reference value $w_{r,A}$ for the initial radial velocity may be obtained from experimental observations in adiabatic annular flow. Andreussi and Azzopardi [46] observed that droplets were ejected in the radial direction with a velocity proportional to the friction velocity of the gas (air). No correlation was found between radial velocity and droplet size. The relationship found by Andreussi and Azzopardi reads:

$$w_{r,A} = 11.1 U^* \sqrt{\frac{\rho_g}{\rho_f}} \quad (34)$$

In the present model, the modules of the droplet initial radial velocities $w_{k,r}$ are taken from a uniform distribution between zero and a maximum value $w_{r,m} = k_r w_{r,A}$, where k_r is a multiplier whose effect has to be investigated by a parametric study. Since the droplets are initially distributed over the entire cross section, it is further assumed that half the droplets travel towards the wall and the others towards the centre.

5.4.4. *Tangential velocity and angular position*. Experimental data on the ejection angle from the wall in the r–ϕ plane are not available. It is, thus, assumed that $w_{k,t}$ has a small value, randomly chosen from a uniform distribution between zero and 0.1 $w_{k,r}$. Such an arbitrary choice is legitimate, as it has a negligible impact on the results, as long as central forces act on the droplets (see Part II). The calculations were performed for $w_{k,t} \neq 0$, since when most of the trajectories do not pass through the centre, the calculation time is reduced. Because of the axisymmetrical nature of the processes considered, the initial angular position $\phi_{k,0}$ of a droplet has no real significance. It is randomly taken from a uniform distribution between 0 and 2π.

6. INTERACTIONS BETWEEN THE PHASES

6.1. *Drag coefficient*

The interfacial drag coefficient is calculated according to the flow regime (viscous or distorted droplets) by well established correlations [19], as long as the droplets are accelerating. For decelerating droplets, the much larger drag coefficients obtained from correlations for fluidized beds are used [47, 48]. Indeed, the axial increase of packing in a decelerating droplet cluster implies contacts between the droplets.

This procedure does not allow large droplets at the quench front to develop negative axial velocities W_z. As a consequence, for low initial vapour velocities, the droplet velocities W_z (and thus also $\langle \alpha_g \rangle$) remain constant (and low) above the quench front, up to the elevation where the increased vapour velocity and the reduced Sauter mean diameter allow acceleration of the droplets. This logic is imposed by the necessity to consider the large (experimentally observed) droplets at the quench front: the more likely physical situation of droplets *oscillating* above the quench front cannot be represented exactly by a steady-state model.

A reasonably smooth transition from decelerating to accelerating flow is achieved by iterating the calculation of the axial velocity until compatibility between velocity difference U_{fg} and C_D is obtained. The logic for selecting the various correlations is discussed by Andreani [16].

6.2. *Interfacial heat transfer coefficient*

The interfacial heat transfer coefficient for a single droplet can be calculated by the correlation of Beard and Pruppacher [49]:

$$h_{0,k} = \frac{k_g}{d_k}(1.56 + 0.616 Re_d^{0.5} Pr_g^{1/3}) \quad (35)$$

where $Re_d \equiv \rho_g |\mathbf{u} - \mathbf{w}| d/\mu_g$ is the droplet Reynolds number and $Pr_g \equiv c_p \mu_g / k_g$ the Prandtl number. The vapour properties are evaluated at T_{eff}, equation (24).

Taking into consideration that interfacial heat transfer is reduced by mass efflux and that the evaporation rate for droplets in a cluster is lower than for

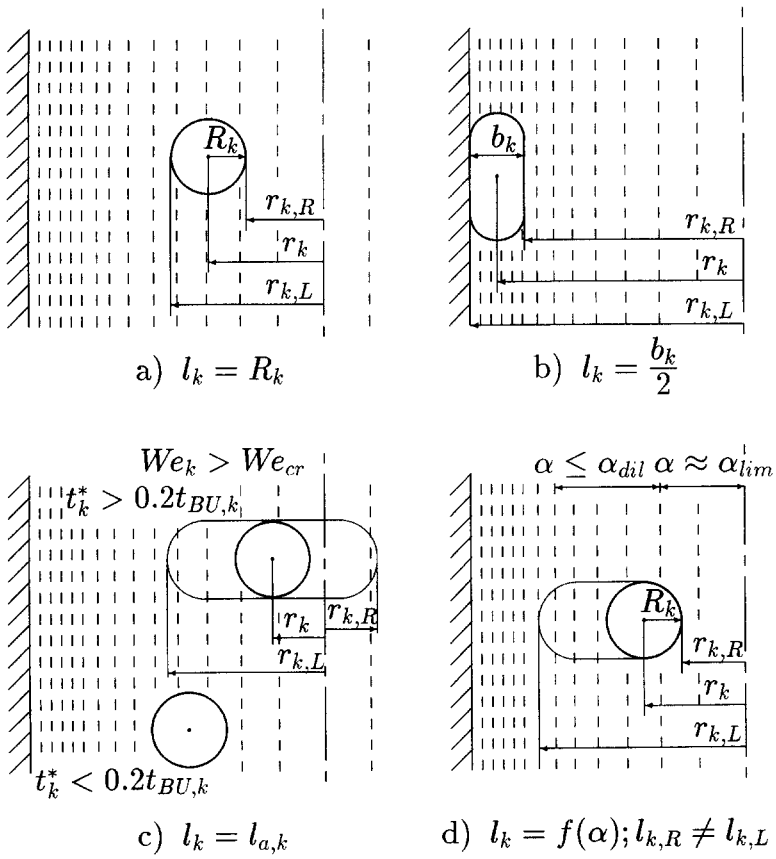

Fig. 8. Partition of the droplet volume among the Eulerian meshes: (a) 'normal case'; (b) droplet in contact with the wall; (c) unstable droplet during aerodynamic break-up; (d) artificial partition to avoid $\alpha_g < \alpha_{lim}$ in the central cells (see text).

isolated droplets, the interfacial heat transfer coefficient for each droplet group k is calculated as:

$$h_{i,k} = h_{0,k} \cdot f_{sh,k} \cdot f_{i,k} \tag{36}$$

where the 'shielding' factor $f_{sh,k}$ is calculated from the correlation of Hoffmann and Ross [50] and the interaction coefficient $f_{i,k}$ is obtained from the correlation of Miura *et al.* [51].

6.3. *Droplet volume partition among the meshes crossed*

The fraction of liquid volume present in each Eulerian cell at a given time can be calculated from the radial position of each droplet given by equations (8) and (9). It is further assumed that the droplet 'extends' by the same length l_k towards the centre ('right boundary' $r_{k,R} = r_k - l_k$) and towards the wall ('left boundary' $r_{k,L} = r_k + l_k$); l_k is the droplet radius (Fig. 8(a)), unless the droplet is in contact with the wall; in this case l_k is the distance between its centre and the wall (Fig. 8(b)). The volume fraction of each droplet is shared among the cells 'covered' by the droplet, proportionally to the participating spacing of the radial mesh, $\Delta r_{k,l}$ (Fig. 2).

The droplet right and left boundaries are calculated differently if the void fraction is very low or if the droplet undergoes aerodynamic break-up.

The droplets which undergo aerodynamic break-up are deformed before breaking and cover a wider cross sectional area than spherical droplets (Fig. 8(c)). The deformation history of the aerodynamically unstable droplets implemented in the model reflects the behaviour observed for droplets breaking in the bag mode [34]. The value of $r_{k,L}$ is limited to the tube radius. Details are given in Fig. 8(c) and by Andreani [16].

Because of the centripetal effect of thrust and lift forces, the droplets tend to group in the centre of the tube (see Part II). As collisions are not taken into account in the model, the liquid volume in the central meshes can exceed the volume of the mesh, resulting in 'negative void fractions'. In order to avoid this unrealistic condition, the droplets are assumed to extend towards the wall as much as necessary to prevent their volume fraction from becoming anywhere higher than the value $\alpha_{f,m} = 0.6$ obtained for closely packed rigid spheres [19]. Thus, the lowest admissible void fraction is $\alpha_{lim} = 1 - \alpha_{f,m}$. An iterative procedure is employed to 'stretch' the left boundary towards the wall for all droplets whose centres lie in a mesh where $\alpha_{g,l} < \alpha_{dil}$ (arbitrarily taken as $\alpha_{lim} + 0.2$). The stret-

ching of $r_{k,I}$ extends up to the first Eulerian mesh where $\alpha_{g,I} > \alpha_{dil}$ (Fig. 8 (d)). This stretching imposes additional iterations regarding the radial position of the droplets.

Resorting to such a 'stretching' of the droplets close to the centre maintains the void fraction above α_{lim} and provides a mechanism mimicking liquid mass diffusion. In reality, at low $\langle\alpha_g\rangle$, the diffusion of liquid towards the periphery of the tube is controlled by the collision rate and the coalescence and break-up phenomena. Binary collisions can result in elastic or inelastic bouncing, permanent coalescence, temporary coalescence or shattering. The outcome depends on both the collision angle and the kinetic energy of the colliding droplets [52]. The description of the real collision–coalescence phenomena at high liquid fractions requires accounting for all the possible events and is beyond the scope of the present work.

The interaction region of a droplet with the vapour field is calculated considering its corrected boundaries. It is clear that the results of analyses where the liquid fraction in some nodes remains close to $\alpha_{f,m}$ over a large portion of the test section have to be considered with some caution. Parametric studies of the influence of $\alpha_{f,m}$ are presented in Part II.

6.4. *Vapour generation rate and distributed heat sink*

Once the evaporation rate for each computational droplet $K_{e,k}$, equations (17)–(27), is known and the volume fraction of the droplet in cells 'covered' is assigned, the total volumetric vapour generation rate can be calculated. From equation (16), the variation of the droplet radius during its residence time Δt in the axial mesh Δz, as well as its total loss of volume ΔV_k can be determined.

The volumetric vapour generation rate in the Eulerian cell between r_{I-1} and r_I is the sum of all the contributions from the droplets that have resided some time $\Delta t_{k,I}$ during Δt in that cell, i.e. the droplets for which the segments (r_{I-1}, r_I) and $(r_{k,L}, r_{k,R})$ overlap for a certain time. Dividing by the volume V_I of that cell:

$$\Gamma_I = \frac{\sum_{k=1}^{N_{GR}} \Delta V_{k,I} \cdot \dot{N}_k}{V_I} \cdot \rho_f \tag{37}$$

where $\Delta V_{k,I}$ is the volume lost by droplet k in the Ith Eulerian radial mesh. A somewhat different distribution scheme is applied to the vapour generated by wall contact (contribution due to q_k^{dc}). Since it is generated on the wall, this vapour source is equally divided among the cells found between the centre of the droplet and the wall.

The distributed interfacial heat sink is calculated in a similar way:

$$-Q_{ig,I} = q'''_{gi,I} = \frac{\sum_{k=1}^{N_{GR}} q_{k,I}^{int} \cdot \Delta t_{k,I} \cdot \dot{N}_k}{V_I} = \frac{\sum_{k=1}^{N_{GR}} \Delta E_{k,I} \cdot \dot{N}_k}{V_I} \tag{38}$$

where $q_{k,I}^{int}$ is the interfacial heat transfer rate from droplet k in the Ith cell (fraction of q_k^{int} given by equation (22)) and $\Delta E_{k,I}$ is the heat exchanged with the vapour during its 'radial' residence time $\Delta t_{k,I}$ in that cell:

$$\Delta E_{k,I} = h_{i,k} \cdot A_{k,I} \cdot \Delta t_{k,I} \cdot (T_I - T_s) \tag{39}$$

$A_{k,I}$ being the fraction of the surface area of the droplet k that is intercepted by mesh I; this is approximated† by $\pi d_k^2 \cdot \Delta r_{k,I}/d_k$.

6.5. *Direct wall–liquid heat transfer*

The total direct heat flux from the wall to the droplets is the sum of the contributions from all the droplets that manage to touch the wall. The contribution of each group k is calculated taking into account the group effectiveness (Section 5.2) and the contact time, $\Delta t_{c,k}$ (equation 10). The total amount of heat extracted by a droplet via direct contact is distributed to the axial meshes involved in proportion to the residence time $\Delta t_{k,J}$ of the droplet in each mesh J. Thus, the direct-contact heat flux for the axial mesh J is:

$$q''_{dc} = \sum_{k=1}^{N_{GR}} \frac{E_k^{dc} \cdot \dot{N}_k \cdot \Delta t_{k,J}}{\Delta t_{c,k}} \cdot \frac{1}{\Delta A_w} = \sum_{k=1}^{N_{GR}} \frac{\varepsilon_k \cdot \rho_f \cdot H_{fg} \cdot \dot{N}_k \cdot V_k \cdot \Delta t_{k,J}}{\Delta t_{c,k}} \cdot \frac{1}{\Delta A_w} \tag{40}$$

where $\dot{N}_k \cdot E_k^{dc}$ is the total power extracted over the contact time.

6.6. *Void fraction*

It can be shown [53] that the liquid fraction in each radial Eulerian mesh I (having volume V_I) can be calculated as the volume occupied during $\Delta t_{k,I}$ by the droplets, divided by V_I. The local void fraction in mesh I becomes:

$$\alpha_{g,I} = 1 - \frac{\sum_{k=1}^{N_{GR}} \dot{N}_k \cdot V_{k,I} \cdot \Delta t_{k,I}}{V_I} \tag{41}$$

where $V_{k,I}$ is the fraction of the volume of droplet k that is intercepted by mesh I. Using again the participating thickness approach, it is approximated‡ by $V_k \Delta r_{k,I}/d_k$. Equations (37), (38), (40) and (41) complement equations (1)–(3), to determine the vapour temperature field.

† Since $A_{k,I}$ changes during $\Delta t_{k,I}$, the actual value of $\Delta E_{k,I}$ is calculated using: $A_{k,I}\Delta t_{k,I} = \Sigma_{p=1}^{N_p} A_{k,I,p}\,dt$, where $dt = \Delta t/N_p$ is the time step used for the integration of equations (8), (9).

‡ The actual calculation uses $V_{k,I} \cdot \Delta_{k,I} = \Sigma_{p=1}^{N_p} V_{k,I,p}\,dt$.

7. NUMERICAL IMPLEMENTATION

The model has been implemented in a computer program: its numerical features are outlined in the present section; more details are given by Andreani [16].

A two-dimensional net is defined for the numerical solution of the vapour conservation equation. The size of the radial meshes is large in the turbulent core (up to 1/10 of the tube diameter) and gradually decreases to the small values required for the laminar sublayer, where the radial meshes are equispaced. The calculations begin at the quench front and advance one axial mesh to step Δz at a time. Since all droplets have the same axial velocity, Δz corresponds to an axial droplet transit time $\Delta t = \Delta z/W_z$. The size of the axial step is controlled by the program [16].

The average axial velocity of the droplets is calculated explicitly only at the bottom of each axial increment from equation (5), since it varies very slowly. The drag coefficient and Sauter mean diameter are considered constant during the advancement, so that the discretized form of the equation (forward differencing) results in an algebraic equation of second degree, which can be solved directly. The calculation is iterated with respect to the drag coefficient, due to the influence of the average void fraction on C_D. The axial velocity is not involved in the global iterative process (external loop, see below), i.e. it is calculated only once for each axial advancement.

The numerical scheme used to solve the set of equations (1)–(3) and (8)–(9), is based on two iterative procedures: an external loop, where the droplet hydrodynamics is calculated with a fixed vapour field, and an internal loop determining the vapour field with droplet variables from the previous external iteration.

To calculate the vapour field, the total vapour generation rate and the new vapour flow rate are first established. Using the imposed two-layer velocity profile and the calculated vapour temperature and density distributions, the new average gas velocity and its radial profile are then established. Iterations are required.

Internal loop

The vapour energy equation is solved by the Keller-Box method [54] using the droplet distribution from the previous elevation. A desirable feature of this method is that it allows the use of a variable radial step size. Moreover, it is unconditionally stable and second-order accurate. The discretized system results in a block tridiagonal matrix that can be directly inverted. The application of the Keller-Box method to the present two-phase problem is illustrated by Andreani [16]. A first-guess radial temperature profile is obtained this way and the new vapour properties are calculated. Equation (1) gives the new average axial velocity, and the new axial velocity distribution is obtained from the two-layer profile. The radial velocities can be calculated from equation (2) with an explicit numerical technique. At this point, equation (3) can be integrated again to give an updated guess for the radial temperature profile and the procedure is repeated until convergence of the internal loop is reached.

External loop

Velocities and positions of the droplets in the r–ϕ plane are updated by integrating equations (8)–(9) over their residence time Δt (equation 20) in the axial mesh Δz. For this integration, the interval Δt is subdivided in time steps of length $\mathrm{d}t$, small enough to avoid that any droplet travels a distance larger than its distance from the wall during $\mathrm{d}t$. Considering lift and thrust forces constant during $\mathrm{d}t$ and neglecting the average velocity of the vapour in the cross-sectional plane, equation (9) can be integrated analytically. The radii of the droplets are calculated by explicit integration of equation (16). After each time step $\mathrm{d}t$, each computational droplet is checked for the occurrence of break-up. If the critical Weber number of a particular break-up process is exceeded, the droplet is 'marked' (in a different way for each of the three different processes), and eventually it splits into new computational droplets (Section 5.3).

The knowledge of the position of the droplets allows to calculate the liquid fraction distribution. If unphysically high droplet packing is detected, the mass of the droplets in the region of high density is redistributed among the adjacent cells (Section 6.3).

The mass sources and heat sinks are then calculated and these values are introduced in the vapour energy equation to get a new temperature distribution (by iteration over the internal loop). Finally, the external loop is repeated until the wall temperature converges.

Verification of the numerical scheme

In order to assess the numerical scheme, single-phase calculations have been carried out and comparisons with analytical or numerical solutions or well-established empirical correlations for both laminar [18, 55] and turbulent [18, 56, 57] flow were performed.

The number of radial nodes in the laminar sublayer was between 10 and 20, while in the turbulent core 20 nodes were sufficient to reach satisfactory accuracy. Excellent agreement with the available solutions was obtained, at least a few diameters above $z = 0$, where the influence of the developing velocity profile is no longer appreciable. The radial mesh used for the two-phase calculations was similar.

The number of radial meshes, as well as the *number of computational droplets* are defined by input values: parametric studies to estimate the influence of such parameters on the calculated results are thus required. Sensitivity studies for two different test conditions (among those considered in Part II) were performed [16]: the first was dominated by wall-impact break-up and the second by aerodynamic break-up. In both cases, both radial mesh NR (30 to 70) and number of

computational droplets *ND* (6–20, per droplet size) had a quite small impact on the calculated wall and vapour temperatures. Moreover, independently of the choice of *NR* and *ND* the global energy balance (*energy input = mixture enthalpy increase*) was preserved: the error was never larger than 2%. This global energy balance has been checked for all the calculations carried out with equally good results.

It can, therefore, be concluded that the results obtained and discussed in the companion paper (Part II) reflect the physics that is imbedded in the model and are not affected by the accuracy of the numerical implementation.

A typical case required ~1 h of CPU time on a CYBER 180-855 computer.

8. CONCLUSION

A novel model specifically assembled to treat in detail the two- and three-dimensional features of the droplet and vapour velocity and temperature fields under typical dispersed flow film boiling conditions was presented. Special emphasis was placed on droplet hydrodynamics. This model will be fully assessed and confronted to several sets of experimental data in the companion paper (Part II).

REFERENCES

1. Andreani, M. and Yadigaroglu, G., Dispersed flow film boiling. An investigation of the possibility to improve the models implemented in the NRC computer codes for the reflooding phase of the LOCA. PSI report No. 51, Paul Scherrer Institute, Villigen, Switzerland, 1989.
2. Yadigaroglu, G. and Andreani, M., Two-fluid modelling of thermal-hydraulic phenomena for best-estimate LWR safety analysis. In *Proceedings of the Fourth International Topical Meeting on Nuclear Reactor Thermal-Hydraulics, NURETH-4*, Vol. 2. AIChE/ANS/ASME, 1989, pp. 980–995.
3. Evans, D. G., Webb, S. W. and Chen, J. C., Measurement of axially varying non-equilibrium in post-critical-heat-flux boiling in a vertical tube. NUREG/CR-3363, Lehigh-University, Bethlehem, PA, 1983.
4. Andreani, M. and Yadigaroglu, G., Prediction methods for dispersed flow film boiling. *International Journal of Multiphase Flow, Annual Reviews*, 1994, **20** (Suppl.), 1–52.
5. Rane, A. G. and Yao, S., Convective heat transfer to turbulent droplet flow in circular tubes. *Journal of Heat Transfer*, 1981, **103**, 679–684.
6. Webb, S. W. and Chen, J. C., A numerical model for turbulent non-equilibrium dispersed flow heat transfer. *International Journal of Heat and Mass Transfer*, 1982, **25**, 325–335.
7. Lin, T. F., Jou, J. F. and Hwang, C. H., Turbulent forced convective heat transfer in two-phase evaporating droplet flow through a vertical pipe. *International Journal of Multiphase Flow*, 1989, **15**, 997–1009.
8. Ganic, E. N. and Rohsenow, W. M., On the mechanism of liquid drop deposition in two-phase dispersed flow. *Journal of Heat Transfer*, 1979, **101**, 288–294.
9. Lee, R. and Almenas, K., Droplet deposition above a quench front during reflooding. *Transactions of the American Nuclear Society*, 1982, **39**, 787–788.
10. Kirillov, P. L., Kashcheyev, V. M., Muranov, Yu. V., and Yuriev, Yu. S., A two-dimensional mathematical model of annular-dispersed and dispersed flows—I. *International Journal of Heat and Mass Transfer*, 1987, **30**, 791–800.
11. Kirillov, P. L., Kashcheyev, V. M., Muranov, Yu. V. and Yuriev, Yu. S., A two-dimensional mathematical model of annular-dispersed and dispersed flows—II. *International Journal of Heat and Mass Transfer*, 1987, **30**, 801–806.
12. James, P. W., Hewitt, G. F. and Whalley, P. B., Droplet motion in two-phase flow. *International Topical Meeting on Nuclear Reactor Thermal-Hydraulics, NUREG/CP-0014*, Vol. 2. ANS/ASME/NRC, 1980, pp. 1484–1503.
13. Govan, A. H., Hewitt, G. F. and Ngan, C. F., Particle motion in a turbulent pipe flow. *International Journal of Multiphase Flow*, 1989, **15**, 471–481.
14. Tsuji, Y., Morkawa, Y. and Terashim, K., Fluid-dynamic interaction between two spheres. *International Journal of Multiphase Flow*, 1982, **8**, 71–82.
15. Kleinstreuer, C. and Wang, T. Y., Approximate analysis of interacting vaporizing fuel droplets. *International Journal of Multiphase Flow*, 1990, **16**, 295–304.
16. Andreani, M., Studies of dispersed flow film boiling with 3-D Lagrangian hydrodynamics and a 2-D Eulerian vapour field. Ph.D. dissertation, Swiss Federal Institute of Technology, Zurich, Switzerland, 1992.
17. Peake, W. T., Dispersed flow film boiling during reflooding. Ph.D. thesis, University of California, Berkeley, CA 1979.
18. Burmeister, L. C., *Convective Heat Transfer*, Wiley, New York, 1983, pp. 468–471, pp. 236–238, p. 486.
19. Ishii, M. and Mishima, K., Two-fluid models and hydrodynamic constitutive relations. *Nuclear Engineering and Design*, 1984, **82**, 107–126.
20. Lawn, C. J., Turbulent heat transfer at low Reynolds numbers. *Journal of Heat Transfer*, 1969, **91**, 532–536.
21. Sun, K. H., Gonzales, J. M. and Tien, C. L., Calculations of combined radiation and convection heat transfer in rod bundles under emergency cooling conditions. ASME paper 75-HT-64, 1975.
22. Watchers, L. H. J. and Westerling, N. A. J., The heat transfer from a hot wall to impinging water drops in the spheroidal state. *Chemical Engineering Science*, 1966, **21**, 1047–1056.
23. Mugele, R. A. and Evans, H. D., Droplet size distribution in sprays. *Industrial & Engineering Chemistry*, 1951, **43**, 1317–1324.
24. Ueda, T., Enomoto, T. and Kanetsuki, M., Heat transfer characteristics and dynamic behavior of saturated droplets impinging on a heated vertical surface. *Bulletin of the JSME*, 1979, **22**, 724–732.
25. Kendall, G. E., Heat transfer to impacting drops and post-critical-heat-flux dispersed flow. Ph.D. thesis, Massachussets Institute of Technology, Cambridge, MA, 1978.
26. Bolle, L. and Moureau, J. Cl., Spray cooling of hot surfaces: a description of the dispersed phase and a parametric study of heat transfer results. In *Two-Phase Flows and Heat Transfer*, Vol. 3, ed. S. Kakac, F. Mayinger and T. N. Veziroglu, Hemisphere, Washington, DC, 1977, pp. 1327–1346.
27. Dukowicz, J. K., A particle-fluid numerical model for liquid sprays. *Journal of Computational Physics*, 1980, **35**, 229–253.
28. Saffman, P. W., The lift on a small sphere in a slow shear flow. *Journal of Fluid Mechanics*, 1965, **22**, 385–400, also *Corrigendum*, 1968, **31**, 624.
29. Rizk, M. A. and Elgobashi, S. E., The motion of a spherical particle suspended in a turbulent flow near a plane wall. *Physics of Fluids*, 1985, **28**, 806–817.
30. Hall, D., Measurements of the mean force on a particle near a boundary in turbulent flow. *Journal of Fluid Mechanics*, 1988, **187**, 451–466.
31. Kendall, G. E. and Rohsenow, W. M., Heat transfer to

dispersed flows and sprays: the liquid contribution. In *Multiphase Transport*, Vol. 2, ed. T. N. Veziroglu. Hemisphere, Washington, 1980, pp. 899–926.
32. Yao, S. C. and Cai, K. Y., The dynamics and Leidenfrost temperature of drops impacting on a hot surface at small angles. ASME paper 85-WA/HT-39, 1985.
33. Ardron, K. H. and Hall, P. C., Droplet hydrodynamics and heat transfer in the dispersed flow regime in bottom reflooding. CEGB report RD/B/5007N81, Berkeley Nuclear Laboratories, London, 1981.
34. Krzeczkowski, S. A., Measurement of liquid droplet disintegration mechanisms. *International Journal of Multiphase Flow*, 1980, **6**, 227–239.
35. Pilch, M. and Erdman, C. A., Use of breakup time data and velocity history data to predict the maximum size of stable fragments for accelerations induced breakup of a liquid drop. *International Journal of Multiphase Flow*, 1987, **13**, 741–757.
36. Irani, R. R., The interpretation of abnormalities in the log-normal distribution of particle size. *Journal of Physical Chemistry*, 1959, **63**, 1603–1607.
37. Podvysotsky, A. M. and Shrayber, A. A., Coalescence and break-up of drops in two-phase flows. *International Journal of Multiphase Flow*, 1984, **10**, 195–209.
38. Sarjeant, M., Drop break-up by gas streams. CEGB report R/M/N1005, Berkeley Nuclear Laboratories, London, 1978.
39. Alad'yev, S. I., Two-phase flows with coalescence and break-up of droplets. *Fluid Mechanics—Soviet Research*, 1975, **4**, 28–34.
40. Kataoka, I., Ishii, M. and Mishima, K., Generation and size distribution of droplets in annular two-phase flow. *Journal of Fluids Engineering*, 1983, **105**, 230–238.
41. Hewitt, G. F. and Hall-Taylor, N. S., *Annular Two-Phase Flow*. Pergamon, Oxford, 1970, pp. 110–120.
42. Ishii, M., One dimensional drift flux model and constitutive equations for relative motion between phases in various two phase flow regimes. Report ANL 77-47, Argonne National Laboratory, Argonne, IL, 1977.
43. Chexal, B. and Lelouche, G., A full range drift flux correlation for vertical flows. EPRI report NP-3989-SR, Electric Power Research Institute, Palo Alto, CA, 1985.
44. Kawaji, M., Transient non-equilibrium two-phase flow: reflooding of a vertical flow channel. Ph.D. thesis, University of California, Berkeley, CA, 1984.
45. Yu, K. P., An experimental investigation of the reflooding of a bare tubular test section. Ph.D. thesis, University of California, Berkeley, CA, 1978.
46. Andreussi, P. and Azzopardi, B., Liquid entrainment in annular two-phase flows. In *Proceedings of the Second International Conference on Liquid Atomization and Spray systems*. Wisconsin, 1982, pp. 209–214.
47. Ergun, S., Fluid flow through packed columns. *Chemical Engineering Progress*, 1952, **48**, 89–94.
48. Wen, C. Y. and Galli, A. F., In *Fluidization*, ed. J. F. Davidson and D. Harrison. Academic Press, London, 1971.
49. Beard, K. V. and Pruppacher, H. R., A wind tunnel investigation of the rate of evaporation of small water drops falling at terminal velocity in air. *Journal of Atmospheric Science*, 1971, **28**, 1445–1464.
50. Hoffmann, T. W. and Ross, L. L., A theoretical investigation of the effect of mass transfer on heat transfer to an evaporating droplet. *International Journal of Heat & Mass Transfer*, 1972, **15**, 599–617.
51. Miura, K., Miura, T. and Ohtani, S., Heat and mass transfer to and from droplet. *AIChE Symposium Series*, 1977, **73**(163), 95–102.
52. Ashgriz, N. and Givi, P., Binary collision dynamics of fuel droplets. *Heat & Fluid Flow*, 1987, **8**, 205–210.
53. Durst, F., Milojevic, D. and Schoenung, B., Eulerian and Lagrangian predictions of particulate two-phase flows: a numerical study. *Applied Mathematical Modelling*, 1984, **8**, 101–115.
54. Keller, K. B., A new difference scheme for parabolic problems. In *Numerical Solutions of Partial Differential Equations*, Vol. 2, ed. B. Hubbard. Academic Press, New York, 1971, pp. 327–350.
55. Worsøe-Schmidt, P. M. and Leppert, G., Heat transfer and friction for laminar flow of gas in a circular tube at high heating rate. *International Journal of Heat Mass Transfer*, 1965, **8**, 1281–1301.
56. Siegel, R. and Sparrow, E. M., Turbulent flow in a circular tube with arbitrary internal heat sources and wall heat transfer. *Journal of Heat Transfer*, 1959, **81**, 280–287.
57. Heineman, J. B., An experimental investigation of heat transfer to superheated steam in round and rectangular tubes. Report ANL-6213, Argonne National Laboratory, Argonne, IL. 1960.